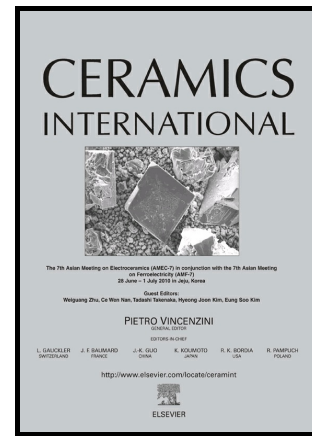


# Author's Accepted Manuscript

Non-isothermal crystallization kinetics for electrospun  $3\text{Al}_2\text{O}_3 \cdot \text{B}_2\text{O}_3 \cdot 2\text{SiO}_2$  ceramic nanofibers prepared using different silica sources

Xiaolei Song, Jing Liu, Juan Wang, Shuwei Yao, Bing Liu, Yunzhu Ma, Wensheng Liu, Qingshan Cai



[www.elsevier.com/locate/ceri](http://www.elsevier.com/locate/ceri)

PII: S0272-8842(18)32556-2  
DOI: <https://doi.org/10.1016/j.ceramint.2018.09.091>  
Reference: CER119490

To appear in: *Ceramics International*

Received date: 29 June 2018  
Revised date: 7 September 2018  
Accepted date: 10 September 2018

Cite this article as: Xiaolei Song, Jing Liu, Juan Wang, Shuwei Yao, Bing Liu, Yunzhu Ma, Wensheng Liu and Qingshan Cai, Non-isothermal crystallization kinetics for electrospun  $3\text{Al}_2\text{O}_3 \cdot \text{B}_2\text{O}_3 \cdot 2\text{SiO}_2$  ceramic nanofibers prepared using different silica sources, *Ceramics International*, <https://doi.org/10.1016/j.ceramint.2018.09.091>

This is a PDF file of an unedited manuscript that has been accepted for publication. As a service to our customers we are providing this early version of the manuscript. The manuscript will undergo copyediting, typesetting, and review of the resulting galley proof before it is published in its final citable form. Please note that during the production process errors may be discovered which could affect the content, and all legal disclaimers that apply to the journal pertain.

**Non-isothermal crystallization kinetics for electrospun  $3\text{Al}_2\text{O}_3\cdot\text{B}_2\text{O}_3\cdot 2\text{SiO}_2$  ceramic  
nanofibers prepared using different silica sources**

*Xiaolei Song, Jing Liu, Juan Wang, Shuwei Yao, Bing Liu, Yunzhu Ma<sup>\*1</sup>, Wensheng Liu<sup>\*1</sup>,  
Qingshan Cai<sup>\*1</sup>*

*State Key Laboratory of Powder Metallurgy, Central South University, Changsha 410083,  
China*

zhuzipm@csu.edu.cn

liuwensheng@csu.edu.cn

caiqingshan@csu.edu.cn

**ABSTRACT:**

In this work, we present a comparative study on the non-isothermal crystallization kinetics for electrospun 3AB2S nanofibers prepared using colloidal silica (CS) and tetraethyl orthosilicate (TEOS) as silica sources. As-spun nanofibers with subequal mean diameters were obtained. Compared with those synthesized through CS, 3AB2S nanofibers prepared using TEOS have higher element homogeneity as a result of the simultaneous hydrolysis of Al and Si. They also show lower crystallinity, smaller mean grain size, higher crystallization temperature and higher activation energy owing to the stronger hindrance effect of uniformly distributed amorphous  $\text{SiO}_2$  on the reaction between  $\text{Al}_2\text{O}_3$  and  $\text{B}_2\text{O}_3$ . Avrami constants values for  $\text{Al}_4\text{B}_2\text{O}_9$  crystallization together with TEM observations reveal an interface-controlled growth mechanism with instantaneous nucleation for both silica sources. However, those

---

<sup>1</sup> Tel.: +86 731 88877825; fax: +86 731 88836800

results indicate a two-dimensional grain growth when CS was used and a three-dimensional grain growth in the case of TEOS.

**Keywords:**

Kinetics; Mullite; Eletrospinning; Silica source

**1. Introduction**

Alumina borates are a kind of important ceramic materials with great industrial importance. It is due to their high melting points, low density and thermal expansion, excellent chemical inertness and mechanical properties, etc. [1,2]. Mullite with the composition of  $3\text{Al}_2\text{O}_3 \cdot 2\text{SiO}_2$  represents another type of ceramic materials for advanced structural and functional applications. They have been widely used in industrial areas because of the excellent dielectric properties, low expansion coefficient and thermal conductivity, good chemical stability, as well as high creep resistance and stability at high temperatures [3]. Based on the advantages of the above two types of ceramics, a new type of ceramics through the combination of alumina borates and mullite would make feasible to inherit the merits of each component material and might even prevail in the overall performance. This idea has raised great research interests in recent years. For instance, Lührs et al. [4] prepared a series of boron doped mullites with starting compositions where  $\text{B}^{3+}$  replaced  $\text{Si}^{4+}$  in equal amounts. The ceramic products retained stable structure after calcining at  $800\text{ }^\circ\text{C}$  for at least 12 days and owned much lower thermal expansion coefficients than 3:2 mullite (the mean value was reduced by 15%). Hong et al. [5] studied the effects of boron doping on grain growth in mullite. They declared that though it lowered the mullite formation temperature, boron benefited the obtainment of a self-reinforcing microstructure because of the significantly

enhanced anisotropic grain growth. Richards et al. [6] found that mullite fibers incorporated with  $B_2O_3$  had smaller grain sizes and deduced that the fibers presented better flexibility and higher tensile strength. Above results ascertain that the ternary ceramics of the combination of alumina borates and mullite have superior performance than each component material, and would be a promising material in high-temperature applications.

It is well known that alumina borate phases ( $Al_4B_2O_9$  and  $Al_{18}B_4O_{33}$ ) appear first in the ternary ceramics due to the reaction between  $Al_2O_3$  and  $B_2O_3$  [4–7]. They retain the main phases only when the  $B_2O_3$  content larger than a certain level. When  $B_2O_3$  content is low, mullite becomes the dominant phase as the temperature increase. Besides,  $SiO_2$  will always be in amorphous state before mullite formation and this amorphous  $SiO_2$  will not vanish as long as alumina borate phases exist. Thus, the ratio of  $Al_2O_3:B_2O_3:SiO_2$  plays an important role in crystallization kinetics and the achievement of high-performance nanocrystalline ceramics. Nextel 312 ceramic fiber with a mol ratio of  $Al_2O_3:B_2O_3:SiO_2$  of 3:1:2 prepared by 3M Company is a typical sample [8–11]. It was found that alumina borate phases are the main crystal phase within a wide temperature range due to the high content of  $B_2O_3$  (14 wt. %). The fibers own excellent flexibility and can be converted into ceramic textiles easily. They can withstand temperatures up to 1400 °C for extended period and up to 1600 °C for short term with little stretching or shrinking. The density of Nextel 312 fiber ( $2.7 \text{ g/cm}^3$ ) is much lower than that of other commercial alumina-based fibers, which is a benefit to reduce the total weight of some equipment when the fibers are used in a large amount.

In recent years, ceramic fibers in nanoscale have received great attention because of the outstanding properties including large surface area, high surface-to-volume ratio, good

flexibility, etc. [12,13]. They have been used as the starting materials to prepare ceramic nanofibrous aerogels, sponges or composites. For example, Si et al. [14] synthesized an ultralight and fire-resistant ceramic aerogels using  $\text{SiO}_2$  nanofibers. Wang et al. [15] fabricated ultralight, scalable, and high-temperature resilient ceramic nanofiber sponges using  $\text{TiO}_2$ ,  $\text{ZrO}_2$ , yttria-stabilized  $\text{ZrO}_2$  and  $\text{BaTiO}_3$  nanofibers. In our previous work, electrospun  $\text{Al}_2\text{O}_3$ - $\text{SiO}_2$ - $\text{B}_2\text{O}_3$  composite nanofibers with better thermal stability than the oxide nanofibers used in Si and Wang's study had been successfully fabricated [16]. They had the same chemical composition with Nextel 312 fibers. We found  $\text{Al}_4\text{B}_2\text{O}_9$  phase at  $900^\circ\text{C}$  and mullite phase at  $1100^\circ\text{C}$ . The nanofibers prepared at  $1000^\circ\text{C}$  showed excellent flexibility. They were uniform and had more stable structure than the majority pure electrospun mullite nanofibers under high temperature circumstance. However, a serious problem in using oxide ceramic nanofibers is that the crystallization and grain growth occur at high temperatures, which will make them become brittle for long-term use. Therefore, it is necessary to understand the crystallization kinetics for the described ternary ceramic nanofibers.

As we know, different silica sources have significant effects on crystallization of pure mullite by means of sol-gel method [17]. Colloidal silica (CS) and tetraethyl orthosilicate (TEOS) are the commonly used silica sources. CS is mixed with alumina sol directly without any post-treatment to prepare diphasic mullite sol. TEOS and alumina sources are usually hydrolyzed simultaneously to acquire monophasic mullite sol. Mullite phase generates at  $\sim 980^\circ\text{C}$  for monophasic gel and forms at  $\sim 1250^\circ\text{C}$  for diphasic gel. Most commercial mullite fibers are produced by CS considering the much higher mullite formation temperatures. However, for  $\text{Al}_2\text{O}_3$ - $\text{SiO}_2$ - $\text{B}_2\text{O}_3$  ternary ceramics with  $\text{Al}_2\text{O}_3$ : $\text{SiO}_2$  mol ratio of 3:2 and high

B<sub>2</sub>O<sub>3</sub> content, whether the use of CS could gain a more stable structure is unknown.

Based on the above discussions, the current work focused on the crystallization kinetics of electrospun 3Al<sub>2</sub>O<sub>3</sub>:B<sub>2</sub>O<sub>3</sub>:2SiO<sub>2</sub> (3AB2S) ceramics nanofibers derived from diphasic and monophasic mullite sols. CS and TEOS were used as the different silica sources. The technical details were given in Sec. 2. In Sec. 3, we presented the results of the synthesized nanofibers through CS and TEOS silica sources. The crystallization kinetics of the nanofibers were discussed in details in Sec. 4. A conclusion was made on the distinct effects of CS and TEOS silica sources on the crystallization kinetics of the 3AB2S nanofibers.

## 2. Experiments

### 2.1. Materials

Tetraethyl orthosilicate (TEOS) with a SiO<sub>2</sub> content of 28 wt. % was bought from Xilong Chemical Co., Ltd. (Guangzhou, China). Commercial colloidal silica (CS) (LUDOX<sup>®</sup> LS) with a SiO<sub>2</sub> content of 30 wt. % was obtained from Sigma-Aldrich (St Louis, USA). Boric acid stabilized aluminum acetate (BAA) (Al(OH)<sub>2</sub>(OOCCH<sub>3</sub>)·1/3H<sub>3</sub>BO<sub>3</sub>) was supplied by Strem Chemicals, Inc. (Boston, USA). PVP (Mw=1,300,000) was provided by Bodi Chemical Reagent Plant (Tianjin, China). Absolute ethanol was purchased from Hengxing Chemical Reagent Co.,Ltd. (Tianjin, China). Deionized water was prepared in the laboratory.

### 2.2. Preparation of 3AB2S ceramic nanofibers

When CS was used, it was mixed with dilute nitric acid (1 wt. %) with a mass ratio of 1:3 to adjust the pH from 8.2 to 4.3 first. After that, BAA was dissolved in deionized water to acquire a 20 wt. % aqueous solution and stirred at 40 °C for 12 h to obtain the alumina sol. The acidulated CS and alumina sol were mixed together to acquire the diphasic sol. When

TEOS was used, BAA, TEOS, deionized water and ethanol were mixed together with mass percentages of 15, 7.2, 38.9 and 38.9 %, respectively. After stirring the mixture at 40 °C for 12 h, a monophasic sol was obtained. It should be noted that though the silica sources were different, the solid contents of the two sols were the same (14.7 wt. %).

PVP powders were dissolved into alcohol to prepare a 16 wt. % PVP alcohol solution. The two sols were mixed with PVP solution with the same mass ratio of 2:3. Then the mixtures were stirred at room temperature for 1 h to obtain the spinning solutions.

Each as-prepared spinning solution was transferred into a plastic syringe equipped with a metallic needle. The needle was connected to a negative voltage supply. Electrospinning and environment parameters for the two spinning solutions were listed in Table. 1. The as-spun nanofibers were collected on aluminum foil and dried at 40 °C for 5 h. Then the dry nanofibers were calcined to 800 °C in air circumstance with a heating rate of 5 °C/min and maintained for 1 h to remove PVP and other organics. After that, they were calcined at 1000 °C for 3 h for microstructure analyses. In the following discussion, the fiber samples prepared using CS and TEOS were labeled as NF<sub>CS</sub> and NF<sub>TEOS</sub>, respectively.

### 2.3. Calculation of crystallization kinetics parameters

The DSC curves of the as-spun nanofibers at heating rates ( $\alpha$ ) of 5, 10, 15 and 20 °C/min were measured to investigate the crystallization processes. Considering that the temperature increases linearly, the crystallized fraction  $\chi$  at temperature  $T$  can be obtained by the following equation:

$$\chi = \frac{1}{\alpha Q_{\text{cryst}} T_s} \int_{T_s}^T \theta dT \quad \text{Eq. (1)}$$

where  $\alpha$  is the heating rate,  $Q_{\text{cryst}}$  is the total crystallization heat,  $T_s$  is the beginning

crystallization temperature and  $\theta$  is the measured heat release rate. Accordingly, the crystallization rate,  $d\chi/dt$ , can be expressed by:

$$\frac{d\chi}{dt} = \frac{\theta}{Q_{cryst}} = \frac{k(T)f(\chi)}{Q_{cryst}} = \frac{k_s f(\chi)}{Q_{cryst}} \exp\left(-\frac{E_a}{RT}\right) \quad \text{Eq. (2)}$$

where  $E_a$  is the activation energy for nucleation-growth of the crystal phase and  $R$  is the gas constant ( $R = 8.314 \text{ J}\cdot\text{mol}^{-1}\cdot\text{K}^{-1}$ ). Eq. (2) demonstrates that the crystallization rate is a product of a  $T$ -dependent reaction rate constant  $k(T)$  and an  $\chi$ -dependent function  $f(\chi)$ . From the exothermic peaks for crystallization obtained at different heating rates, the activation energy  $E_a$  for nucleation-growth of the crystal phase can be calculated by the Kissinger equation [18]:

$$\ln\left(\frac{T_p^2}{\alpha}\right) = \frac{E_a}{RT_p} + const \quad \text{Eq. (3)}$$

where  $T_p$  is the exothermic peak temperature. Plotting  $\ln(T_p^2/\alpha)$  versus  $1/T_p$  yields the  $E_a$  value. The crystallization process for the ceramic nanofibers is interpreted in terms of the classical Johnson-Mehl-Avrami (JMA) kinetic model [19–21]. In this model, the relationship between the crystallized fraction  $\chi$  and time  $t$  at a constant heating rate is given in the following form:

$$\chi = 1 - \exp\left[-\left(k(T)\frac{T-T_s}{\alpha}\right)^n\right] \quad \text{Eq. (4)}$$

where  $n$  is the Avrami exponent. To acquire the  $n$  value, the Ozawa's method is adopted [22].

Taking twice the logarithm of Eq. (4) can obtain the following relationship:

$$\ln[-\ln(1-\chi)] = n \ln k(T) + n \ln(T-T_s) - n \ln \alpha \quad \text{Eq. (5)}$$

In Eq. (5),  $n \ln k(T) + n \ln(T-T_s)$  is a constant at a constant temperature, thus plotting  $\ln[-\ln(1-\chi)]$  versus  $\ln \alpha$  (where  $\chi$  values are acquired at the same temperature in DSC curves taken at different heating rates) gives straight lines. From the slope of each line, the value of

Avrami exponent  $n$  is obtained. The  $n$  value, which determines the crystallization mechanism, can be expressed as  $n = a + mb$ , where  $a$  corresponds to the nucleation rate (0 for a zero nucleation rate,  $0 < a < 1$  for a decreasing nucleation rate and 1 for a constant nucleation rate),  $m$  relates to the growth dimensionality (3 for three-dimensional growth, 2 for two-dimensional growth and 1 for one-dimensional growth), and  $b$  refers to the growth mechanism (0.5 for a diffusion-controlled mechanism and 1 for an interface-controlled mechanism) [23].

## 2.4. Characterization

The morphology of the nanofibers was examined by Quanta FEG 250 scanning electron microscopy (SEM) (FEI, USA). The elemental line scan analyses was acquired using energy dispersive X-ray spectroscopy (EDS) equipped on Titan G2 60-300 transmission electron microscopy (FEI, USA). The microstructure of the crystallized fibers was observed by JEM-2100F transmission electron microscopy (TEM) (JEOL, Japan). Fiber diameters and grain sizes were calculated using image analysis software (Image J). Differential scanning calorimetry (DSC) analyses of the as-spun nanofibers were performed on STA-449C thermoanalyzer (Netzsch, German) in air atmosphere. The phase composition of the calcined nanofibers was determined by D8 Advance X-ray powder diffractometer (XRD) (Bruker, German) with  $\text{CuK}\alpha$  radiation in the region of  $10 < 2\theta < 70^\circ$ .

## 3. Results

### 3.1 Electrospun 3AB2S nanofibers

Fig.1 displays the SEM micrographs and diameter distribution histograms for as-spun nanofibers. As observed from Fig.1 (a) and (c), the nanofibers were continuous and uniform

and the surface was smooth for both samples. The diameter distribution histograms (Fig.1 (b) and (d)) showed that the average diameters were  $851 \pm 96$  nm and  $865 \pm 64$  nm, respectively. The subequal diameters was a desired result for an accurate and reliable comparative study because it could eliminate the influence of fiber diameters on the crystallization behavior.

HAADF STEM micrographs and EDS line scan analyses for 3AB2S nanofibers obtained at 800 °C are shown in Fig. 2. The HAADF STEM micrographs (Fig. 2(a) and (c)) showed that the fiber-like structure retained and no chalking phenomenon occurred in the two samples after calcining treatment. Since the samples were in amorphous state, we suppose that the amorphous  $\text{Al}_2\text{O}_3$ ,  $\text{SiO}_2$  and  $\text{B}_2\text{O}_3$  particles scattered homogeneously.

For the two sols, boric acid scattered uniformly because it did not participate in the hydrolysis and condensation reactions. Al and Si were mixed at nanometer level when CS was used and at atomic level when TEOS was used according to the synthetic routes. Therefore, lower homogeneity of Al, Si, B and O elements in amorphous  $\text{NF}_{\text{CS}}$  was expected. The EDS line scans confirmed such assumption. As shown in Fig. 2(b), the element distribution curves were uneven. The distribution of Al and Si along the axial direction changed in an opposite trend. That was, at the positions with high Al content, the Si content was low, and vice versa. From the distances between two nearby crests of Al, Si and B, it could be concluded that the amorphous oxide particles in  $\text{NF}_{\text{CS}}$  were mixed in nanoscale. By contrast, the curves displayed in Fig. 2(d) were relatively even. Some regions in the curves of Al and Si showed similar fluctuation, indicating that Al and Si were mixed in atomic level.

XRD patterns of 3AB2S nanofibers prepared using CS and TEOS after calcining at 1000 °C for 3 h are displayed in Fig. 3. The crystal phases were all confirmed as  $\text{Al}_4\text{B}_2\text{O}_9$

phase for the two samples. The broad humps located between the  $2\theta$  of  $13^\circ$  and  $29^\circ$  were all identified as amorphous  $\text{SiO}_2$ . Though the crystal phases were the same for both samples, the intensities of the diffraction peaks were not. Higher intensities were observed for  $\text{NF}_{\text{CS}}$ , suggesting a higher crystallinity.

Fig. 4 shows the TEM micrographs and grain size distribution histograms of 3AB2S nanofibers. It could be seen from Fig. 4(a) and (c) that the majority of the crystal grains presented in the inner of the fibers and were surrounded by amorphous  $\text{SiO}_2$ . A few grains grew to the surface and deteriorated the surface morphology. The grains in  $\text{NF}_{\text{TEOS}}$  were in spherical, ellipsoidal and elongated shapes, and distributed uniformly. While the grains in  $\text{NF}_{\text{CS}}$  were less, irregular and nonuniformly distributed. The grain size distribution histograms in Fig. 4(b) and (d) showed that the average sizes were  $39 \pm 14$  nm and  $16 \pm 7$  nm for  $\text{NF}_{\text{CS}}$  and  $\text{NF}_{\text{TEOS}}$ , respectively. To summarize, 3AB2S nanofibers prepared using TEOS had grains with larger quantity, smaller size, narrower size range, regular shapes and uniformly distributed feature.

### 3.2 Non-isothermal Crystallization kinetics

The DSC curves of crystalline region for the two as-spun nanofibers measured at various heating rates are displayed in Fig. 5. The start ( $T_s$ ), peak ( $T_p$ ) and end ( $T_e$ ) temperatures for crystallization can be seen in Table 2. All the crystallization peaks were ascribed to the formation of  $\text{Al}_4\text{B}_2\text{O}_9$  phase.  $T_s$ ,  $T_p$  and  $T_e$  for the two samples shifted to higher values as the heating rate increased. This was a typical tendency for glasses or ceramics under the non-isothermal crystallization. The thermal lag effect of heating rate on crystallization was responsible for it. That was, a slower heating rate could offer more sufficient time to activate

nucleation at a lower temperature, but a faster heating rate could not. Beyond that, the  $T_p$  values for NF<sub>CS</sub> were lower than that for NF<sub>TEOS</sub> at the same heating rate (e.g. at 10 °C/min, NF<sub>CS</sub>: 900.6 °C; NF<sub>TEOS</sub>: 910.7 °C). Such a result revealed that though it did not participate in the reaction of forming Al<sub>4</sub>B<sub>2</sub>O<sub>9</sub> phase, SiO<sub>2</sub> did affect the crystallization process.

According to Eq(1) and Eq(2), the crystallized fraction  $\chi$  and the crystallization rate  $d\chi/dt$  as a function of temperature  $T$  at various heating rates for the two fiber samples are acquired and displayed in Fig. 6 and 7. The characteristic values are also listed in Table 2. All the plots of  $\chi$  versus  $T$  had similar sigmoidal shapes, which were in line with the classical curves for glass or ceramics [24]. When the heating rate increased, the crystallization temperature range ( $T_e-T_s$ ) enlarged, the total crystallization time  $t$  ( $t = (T_e-T_s)/\alpha$ ) shortened, and the crystallization rates ( $d\chi/dt$ ) increased. Thus higher values of maximum crystallization rate ( $(d\chi/dt)_{\max}$ ) were obtained. Moreover, lower  $t$  values generated on the basis of same heating rates for NF<sub>TEOS</sub>, which indicated the shorter times for the completion of crystallization and higher  $d\chi/dt$  values during crystallization. Apart from that, the  $d\chi/dt$  values were much lower at the beginning and ending period of the crystallization process, implying that the reaction between Al<sub>2</sub>O<sub>3</sub> and B<sub>2</sub>O<sub>3</sub> proceeded slightly.

Fig. 8 shows the plots of  $\ln(T_p^2/\alpha)$  versus  $1/T_p$  for the two 3AB2S nanofibers. As could be seen, two linear plots were acquired, revealing the validity of the Kissinger method and the corresponding assumptions. The obtained  $E_a$  values for NF<sub>CS</sub> and NF<sub>TEOS</sub> as listed in Table 3 were  $607 \pm 17$  kJ/mol and  $662 \pm 24$  kJ/mol, respectively. Fig. 9 shows the plots of  $\ln[-\ln(1-\chi)]$  versus  $\ln\alpha$  for the crystalline regions of the 3AB2S nanofibers. The Avrami constant  $n$ , as well as  $a$ ,  $m$  and  $b$ , were calculated and listed in Table 3. For NF<sub>CS</sub>, the Avrami constant  $n$  was 2.6,

pointing to a decreasing nucleation rate of  $\text{Al}_4\text{B}_2\text{O}_9$  phase, the two-dimensional growth of crystal grains and an interface-controlled growth mechanism. The  $n$  value for  $\text{NF}_{\text{TEOS}}$  was 3.6, revealing that the crystal growth was the three-dimensional type and the growth process was controlled by reactions at the phase boundaries. Since  $a$  value was not zero, the nucleation also proceeded to some certain during the crystal growth process.

## 4. Discussion

### 4.1 Activation energies for 3AB2S ceramic nanofibers

The effects of a small amount of boron on the crystallization kinetics of mullite had been well studied in the literature [25,26]. Nevertheless, a systematic investigation on the crystallization kinetics for  $\text{Al}_2\text{O}_3$ - $\text{SiO}_2$ - $\text{B}_2\text{O}_3$  ternary ceramics with  $\text{Al}_2\text{O}_3$ : $\text{SiO}_2$  mol ratio of 3:2 and high content of  $\text{B}_2\text{O}_3$  are lacking. In present work, the activation energies of  $607 \pm 17$  kJ/mol and  $662 \pm 24$  kJ/mol were obtained for  $\text{NF}_{\text{CS}}$  and  $\text{NF}_{\text{TEOS}}$ , respectively, which are much higher than those of  $\text{Al}_2\text{O}_3$ - $\text{B}_2\text{O}_3$  binary systems. For instance, O. Yamaguchi *et al.* [27] reported the formation kinetics of  $\text{Al}_4\text{B}_2\text{O}_9$  phase for  $\text{B}^{3+}$ -substituted boehmite gel and found an activation energy of 368 kJ/mol. The presence of  $\text{SiO}_2$  was regarded as the reason for the high activation energy of 3AB2S fibers. The amorphous  $\text{SiO}_2$  could delay the reaction between  $\text{Al}_2\text{O}_3$  and  $\text{B}_2\text{O}_3$  due to the hindrance effect. Besides, the viscosity of glass phase in  $\text{Al}_2\text{O}_3$ - $\text{SiO}_2$ - $\text{B}_2\text{O}_3$  ternary ceramics might be higher than that in  $\text{Al}_2\text{O}_3$ - $\text{B}_2\text{O}_3$  binary ceramics [7,28], which made the diffusion of Al and B atoms sluggish. All these results led to the higher  $E_a$  values for  $\text{Al}_4\text{B}_2\text{O}_9$  phase in 3AB2S ceramic nanofibers.

We did not find any exothermic peaks in the DSC curves in the range of 1000-1400 °C for the two fibers (figures not shown here), which indicated no phase transformations at this

temperature range. However, it is well known that two new phases,  $\text{Al}_{18}\text{B}_4\text{O}_{33}$  and mullite, formed when  $\text{Al}_2\text{O}_3\text{-SiO}_2\text{-B}_2\text{O}_3$  ternary ceramics were calcined at temperatures higher than  $1000\text{ }^\circ\text{C}$  [4,7,29]. Most researchers found that the heat releasing for  $\text{Al}_{18}\text{B}_4\text{O}_{33}$  and mullite indeed occur during their formation processes. For instance, exothermic peaks corresponded to  $\text{Al}_{18}\text{B}_4\text{O}_{33}$  formation could be detected for  $\text{Al}_2\text{O}_3\text{-B}_2\text{O}_3$  binary ceramics [30]. Mullite formation temperatures could be derived by DTA analyses for diphasic 3:2 mullite with 5 wt. %  $\text{B}_2\text{O}_3$  [5]. For monophasic 3:2 mullite with 6.14 wt. %  $\text{B}_2\text{O}_3$ , the exothermic peaks for mullite phase could also be observed [7]. Above results raise an interesting question that why we did not observe the exothermic peaks on the DSC curves.

We reckoned the absence of exothermic peaks on the DSC curves would be ascribed as the second-order phase transformation nature from  $\text{Al}_4\text{B}_2\text{O}_9$  to  $\text{Al}_{18}\text{B}_4\text{O}_{33}$  or mullite. As we know,  $\text{Al}_4\text{B}_2\text{O}_9$ ,  $\text{Al}_{18}\text{B}_4\text{O}_{33}$  and mullite had same crystal structure and similar lattice parameters (listed in Table 4). No variation in crystal structure and no significant changes in lattice parameters took place during the phase transition process.  $\text{Al}_{18}\text{B}_4\text{O}_{33}$  generated *in situ* from the decomposition of  $\text{Al}_4\text{B}_2\text{O}_9$ , and alumina borate phases acted as epitaxial substrates for mullite nucleation and growth [5,26]. Because of the much larger content of boron in 3AB2S ceramics (14 wt. %), the nucleation process for  $\text{Al}_{18}\text{B}_4\text{O}_{33}$  and mullite might not occur once  $\text{Al}_4\text{B}_2\text{O}_9$  formed. In this case, the crystallization heat is consecutive for this second-order phase transitions, and consequently, was difficult to be detected. Therefore, to study the kinetics of phase transformation from  $\text{Al}_4\text{B}_2\text{O}_9$  to  $\text{Al}_{18}\text{B}_4\text{O}_{33}$  and the kinetics of mullite formation in 3AB2S nanofibers by DSC analyses was unsuitable.

Besides, it should be noted that most diffraction lines of the three phases overlapped [7],

i.e. to ascertain their amounts by XRD measurement was unfathomable. As a consequence, the crystallization kinetics for  $\text{Al}_{18}\text{B}_4\text{O}_{33}$  and mullite could not be acquired by XRD either.

#### 4.2 Effects of silica sources on crystallization

We now turn to having the discussion of the hindrance effects of amorphous  $\text{SiO}_2$  on the reaction of  $\text{Al}_2\text{O}_3$  and  $\text{B}_2\text{O}_3$ . Since the solid contents of the two precursor sols and the dosage of PVP in the two spinning solutions were same, the effects of PVP contents on crystallization were negligible [30,31]. As deduced by EDS line scans, particles of  $\text{Al}_2\text{O}_3$  and  $\text{B}_2\text{O}_3$  in  $\text{NF}_{\text{TEOS}}$  were smaller and better separated by amorphous  $\text{SiO}_2$  than those in  $\text{NF}_{\text{CS}}$ . The hindrance effect of  $\text{SiO}_2$  was stronger for  $\text{NF}_{\text{TEOS}}$ , and consequently, higher  $T_p$  values and  $E_a$  values were acquired.

In addition, crystallized  $\text{NF}_{\text{TEOS}}$  owned lower crystallinity and more crystal grains, implying that more nucleation sites generated during the crystallization process. Only amorphous  $\text{Al}_2\text{O}_3$  and  $\text{B}_2\text{O}_3$  particles closed to the nucleation sites participated into the growth process because the crystallization was conducted by interface-controlled growth mechanism. When the nucleation sites grew to grains, larger area of grain boundaries formed and more energy was required for the coalescence of grains under high temperatures. All these results led to a lower grain growth rate. The  $m$  values showed that grains grew in two dimensions in  $\text{NF}_{\text{CS}}$  and grew in three dimensions in  $\text{NF}_{\text{TEOS}}$ . Such result was verified by the TEM observation (Fig. 4) that regular grains formed in  $\text{NF}_{\text{TEOS}}$  while irregular ones generated in  $\text{NF}_{\text{CS}}$ . To summarize, it could be concluded that 3AB2S nanofibers prepared using TEOS had better thermal stability.

## 5. Conclusions

The crystallization kinetics for electrospun 3AB2S nanofibers prepared by two silica sources (colloidal silica (CS) and tetraethyl orthosilicate (TEOS)) were obtained under non-isothermal conditions. The results showed that the fibers prepared by CS had much lower element homogeneity than those prepared by TEOS. After calcining at 1000 °C, the two fibers were composed of  $\text{Al}_4\text{B}_2\text{O}_9$  and amorphous  $\text{SiO}_2$ . The crystallized  $\text{NF}_{\text{TEOS}}$  had lower crystallinity, more grains, smaller grain sizes and more regular grain shapes than the counterpart. The formation temperatures of  $\text{Al}_4\text{B}_2\text{O}_9$  for  $\text{NF}_{\text{TEOS}}$  were at least 9 °C higher than that for  $\text{NF}_{\text{CS}}$ . During the crystallization process, the crystallization rate for  $\text{NF}_{\text{TEOS}}$  was higher than that of  $\text{NF}_{\text{CS}}$ , revealing the higher nucleation rate and lower grain growth rate. The  $E_a$  for  $\text{NF}_{\text{CS}}$  and  $\text{NF}_{\text{TEOS}}$  were  $607 \pm 17$  kJ/mol and  $662 \pm 24$  kJ/mol, respectively. For both samples, nucleation rates decreased during heating and the reactions at phase boundaries controlled the crystal growth after nucleation. Crystal grains grew in two dimensions in  $\text{NF}_{\text{CS}}$  while in three dimensions in  $\text{NF}_{\text{TEOS}}$ . This distinct microstructure and crystallization of  $\text{NF}_{\text{CS}}$  and  $\text{NF}_{\text{TEOS}}$  were ascribed to the different hindrance effects of amorphous  $\text{SiO}_2$  on the reaction between  $\text{Al}_2\text{O}_3$  and  $\text{B}_2\text{O}_3$ . We also revealed that DSC method was unsuitable for studying the kinetics of transformation from  $\text{Al}_4\text{B}_2\text{O}_9$  to  $\text{Al}_{18}\text{B}_4\text{O}_{33}$  and formation of mullite for 3AB2S nanofibers, since no crystallization peak of  $\text{Al}_{18}\text{B}_4\text{O}_{33}$  or mullite was detected.

## Acknowledgements

The authors gratefully acknowledge the financial support from the “Chang Jiang Scholars Program” of the Ministry of Education of China (Grant no. T2011119).

**References:**

- [1] X. Tao, X. Wang, X. Li, Nanomechanical Characterization of One-Step Combustion-Synthesized  $\text{Al}_4\text{B}_2\text{O}_9$  and  $\text{Al}_{18}\text{B}_4\text{O}_{33}$  Nanowires, *Nano Lett.* 7 (2007) 3172–3176.
- [2] P. Gielisse, W. Foster, The system  $\text{Al}_2\text{O}_3\text{-B}_2\text{O}_3$ , *Nature.* 195 (1962) 69–70.
- [3] H. Schneider, Basic Properties of Mullite, in H. Schneider, S. Komarneni (Eds.), *Mullite*, Wiley-VCH, Weinheim, 2005, pp. 141-215.
- [4] H. Lührs, R.X. Fischer, H. Schneider, Boron mullite: Formation and basic characterization, *Mater. Res. Bull.* 47 (2012) 4031–4042.
- [5] S.H. Hong, W. Cermignani, G.L. Messing, Anisotropic Grain Growth in Seeded and  $\text{B}_2\text{O}_3$ -doped Diphasic Mullite Gels, *J. Eur. Ceram. Soc.* 16 (1996) 133–141.
- [6] E.A. Richards, C.J. Goodbrake, H.G. Sowman, Reactions and Microstructure Development in Mullite Fibers, *J. Am. Ceram. Soc.* 74 (1991) 2404–2409.
- [7] G. Zhang, Z. Fu, Y. Wang, H. Wang, W. Wang, J. Zhang, S.W. Lee, K. Niihara, Boron-doped mullite derived from single-phase gels, *J. Eur. Ceram. Soc.* 30 (2010) 2435–2441.
- [8] D. D. Johnson, NEXTEL 312 CERAMIC FIBER FROM 3M, *J. Ind. Text.* 10 (1982) 282-296.
- [9] A.R. Bunsell, M.H. Berger, Fine diameter ceramic fibres, *J. Eur. Ceram. Soc.* 20 (2000) 2249–2260.
- [10] T.L. Tompkins, Ceramic oxide fibers: building blocks for new applications, *Ceram. Ind.* 144 (1995) 45-48.

- [11] H. G. Sowman. Alumina–boria–silica ceramic fibers from the sol-gel process, in: L. C. Klein, (Eds.), Sol-gel technology for thin films, fibers, performs, electronics, and specialty shapes, Park Ridge, NJ, 1988, pp. 162–82.
- [12] H. Wu, W. Pan, D. Lin, H. Li, Electrospinning of ceramic nanofibers: Fabrication, assembly and applications, *J. Adv. Ceram.* 1 (2012) 2–23.
- [13] D. Li, J.T. McCann, Y. Xia, M. Marquez, Electrospinning: A simple and versatile technique for producing ceramic nanofibers and nanotubes, *J. Am. Ceram. Soc.* 89 (2006) 1861–1869.
- [14] Y. Si, X. Wang, L. Dou, J. Yu, B. Ding, Y. Huang, C. Zhao, Ultralight and fire-resistant ceramic nanofibrous aerogels with temperature-invariant superelasticity, *Sci. Adv.* 4.4 (2018).
- [15] H. Wang, X. Zhang, N. Wang, Y. Li, X. Feng, Y. Huang, C. Zhao, Ultralight, scalable, and high-temperature-resilient ceramic nanofiber sponges, *Sci. Adv.* 3. 6 (2017).
- [16] X. Song, W. Liu, S. Xu, J. Wang, B. Liu, Q. Cai, S. Tang, Y. Ma, Microstructure and elastic modulus of electrospun  $\text{Al}_2\text{O}_3\text{-SiO}_2\text{-B}_2\text{O}_3$  composite nanofibers with mullite-type structure prepared at elevated temperatures, *J. Eur. Ceram. Soc.* 38 (2018) 201–210.
- [17] L.S. Cividanes, T.M.B. Campos, L.A. Rodrigues, D.D. Brunelli, G.P. Thim, Review of mullite synthesis routes by sol-gel method, *J. Sol-Gel Sci. Technol.* 55 (2010) 111–125.
- [18] H.E. Kissinger, Reaction Kinetics in Differential Thermal Analysis, *Anal. Chem.* 29 (1957) 1702–1706.

- [19] S.O. Kasap, C. Juhasz, Theory of thermal analysis of non-isothermal crystallization kinetics of amorphous solids, *J. Chem. Soc. Faraday Trans. 2.* 81 (1985) 811-831.
- [20] A.T.W. Kempen, F. Sommer, E.J. Mittemeijer, Determination and interpretation of isothermal and non-isothermal transformation kinetics; The effective activation energies in terms of nucleation and growth, *J. Mater. Sci.* 37 (2002) 1321–1332.
- [21] J. Málek, Kinetic analysis of crystallization processes in amorphous materials, *Thermochim. Acta.* 355 (2000) 239–253.
- [22] T. Ozawa, Kinetics of non-isothermal crystallization, *Polymer.* 12 (1971) 150–158.
- [23] Y.M. Sung, Nonisothermal phase formation kinetics in sol-gel-derived strontium bismuth tantalate, *J. Mater. Res.* 16 (2001) 2039–2044.
- [24] B.J.L.M. Rupp, B. Scherrer, A.S. Harvey, J. Gauckler, Crystallization and Grain Growth Kinetics for Precipitation-Based Ceramics : A Case Study on Amorphous Ceria Thin Films from Spray Pyrolysis, (2009) 2790–2799.
- [25] M. Schmücker, F. Flucht, H. Schneider, High Temperature Behaviour of Polycrystalline Aluminosilicate Fibres with Mullite Bulk Composition. II. Kinetics of Mullite Formation, *J. Eur. Ceram. Soc.* 16 (1996) 281–285.
- [26] S.H. Hong, G.L. Messing, Mullite Transformation Kinetics in  $P_2O_5$ -,  $TiO_2$ -, and  $B_2O_3$ -Doped Aluminosilicate Gels, *J. Am. Ceram. Soc.* 80 (1997) 1151–1159.
- [27] O. Yamaguchi, M. Tada, K. TakeoKa, K. Shimizu, Kinetics on the formation and decomposition of  $2Al_2O_3 \cdot B_2O_3$  from mixed powders prepared by the alkoxy-method, *B. Chem. Soc. Jpn* 52 (1979) 2153–2154.
- [28] N.P. Bansal, R.H. Doremus. Handbook of glass properties. New York: Academic Press;

1986.

- [29] X. Dong, G. Sui, A. Guo, H. Du, J. Liu, Synthesis and properties of lightweight flexible insulant composites with a mullite fiber-based hierarchical heterostructure, *Chem. Eng. J.* 277 (2015) 159–167.
- [30] X. Song, W. Liu, J. Wang, S. Xu, B. Liu, J. Liu, Y. Ma, Microstructural differences between electrospun alumina borate nanofibers prepared by solutions with different PVP contents, *Ceram. Int.* 43 (2017) 9831–9837.
- [31] J. Leivo, M. Lindén, J.M. Rosenholm, M. Ritola, C. V. Teixeira, E. Levänen, T.A. Mäntylä, Evolution of aluminosilicate structure and mullite crystallization from homogeneous nanoparticulate sol-gel precursor with organic additives, *J. Eur. Ceram. Soc.* 28 (2008) 1749–1762.

**Fig. 1.** SEM micrographs and diameter distribution histograms for as-spun nanofibers: (a) (b)  $\text{NF}_{\text{CS}}$  and (c) (d)  $\text{NF}_{\text{TEOS}}$ . The inserts show the surface morphology.

**Fig. 2.** HAADF STEM micrographs and EDS line scan analyses for 3AB2S nanofibers prepared at 800 °C: (a) (b)  $\text{NF}_{\text{CS}}$  and (c) (d)  $\text{NF}_{\text{TEOS}}$ .

**Fig. 3.** XRD patterns of 3AB2S nanofibers prepared using different sources after calcining at 1000 °C for 3 h.

**Fig. 4.** TEM micrographs and grain size distribution histograms for 3AB2S nanofibers: (a) (b)  $\text{NF}_{\text{CS}}$  and (c) (d)  $\text{NF}_{\text{TEOS}}$ .

**Fig. 5.** DSC curves of crystalline region for as-spun nanofibers measured at various heating rates: (a)  $\text{NF}_{\text{CS}}$  and (b)  $\text{NF}_{\text{TEOS}}$ .

**Fig. 6.** The relationships between  $\chi$  and  $T$  for 3AB2S nanofibers under different heating rates: (a) NF<sub>CS</sub> and (b) NF<sub>TEOS</sub>.

**Fig. 7.** The relationships between  $d\chi/dt$  and  $T$  for 3AB2S nanofibers under different heating rates: (a) NF<sub>CS</sub> and (b) NF<sub>TEOS</sub>.

**Fig. 8.** Plots of  $\ln(T_p^2/\alpha)$  versus  $1/T_p$  for the 3AB2S nanofibers prepared using CS and TEOS.

**Fig. 9.** Plots of  $\ln[-\ln(1-\chi)]$  versus  $\ln\alpha$  for the crystalline regions of the 3AB2S nanofibers prepared using CS and TEOS.

**Table 1:** Electrospinning and environment parameters for the spinning solutions prepared using different silica sources.

Silica source	Electrospinning parameters			Environment parameters	
	Voltage (kV)	Distance (cm)	Feeding rate (mL/h)	Temperature (°C)	Humidity (%)
CS	-6.0	15	0.25	32-35	20-25
TEOS	-7.45	15	0.45	22-25	50-55

**Table 2:** Characteristic values of crystallization for 3AB2S nanofibers determined from non-isothermal analysis at different heating rates.

Silica sources	$\alpha$ (°C/min)	$T_s$ (°C)	$T_p$ (°C)	$T_e$ (°C)	$T_e - T_s$ (°C)	$t$ (s)	$10^3(d\chi/dt)_{\max}$ (s <sup>-1</sup> )
	CS	5	873	885	898	25	300

	10	886.5	901	920	33.5	201	16.34
	15	895	907	928	33	132	27.30
	20	901.5	913	937	35.5	106.5	36.64
TEOS	5	886	897	906	20	240	13.30
	10	898	911	924.5	26.5	159	22.26
	15	907	918	934.5	27.5	110	35.53
	20	910	923	940	30	90	41.98

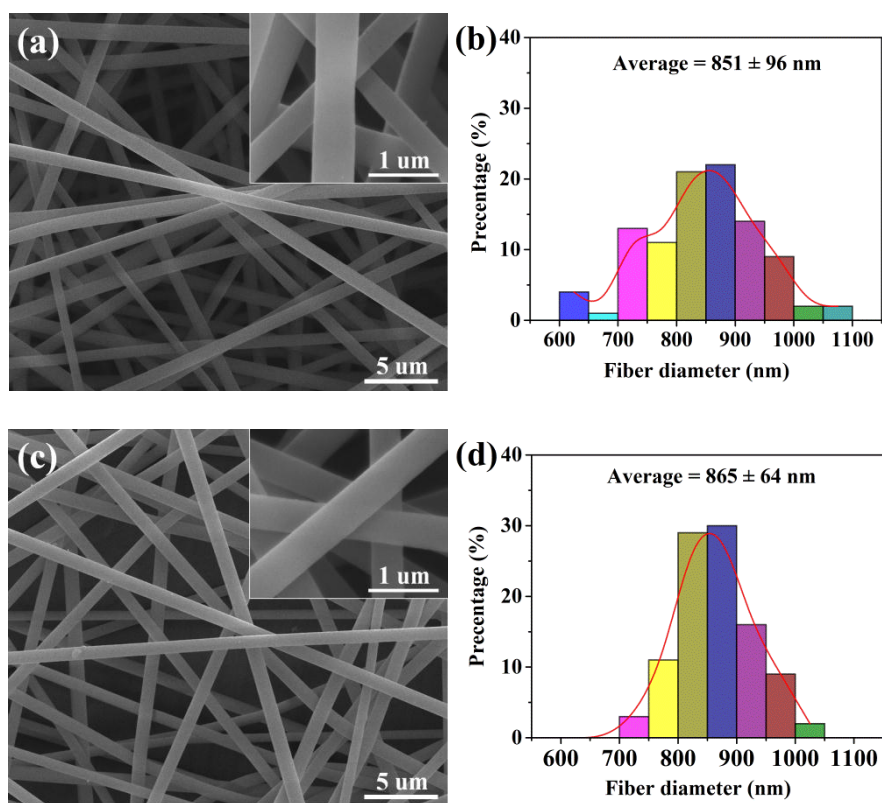
**Table 3:** Activation energies ( $E_a$ ) and Avrami constants ( $n$ ) for nucleation-growth of  $\text{Al}_4\text{B}_2\text{O}_9$  phase from 3AB2S nanofibers calculated by the Kissinger method.

Silica source	$E_a$ (kJ/mol)	$n$	$a$	$m$	$b$
CS	$607 \pm 17$	2.6	0.6	2	1
TEOS	$662 \pm 24$	3.6	0.6	3	1

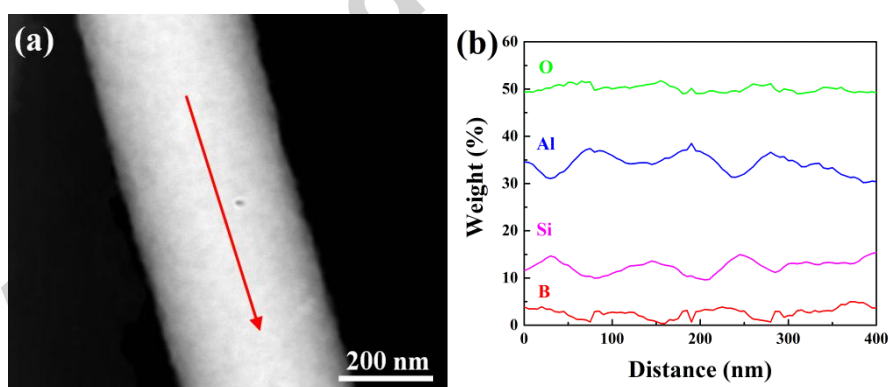
**Table 4:** Crystal structure and lattice parameters of  $\text{Al}_4\text{B}_2\text{O}_9$ ,  $\text{Al}_{18}\text{B}_4\text{O}_{33}$  and mullite phase.

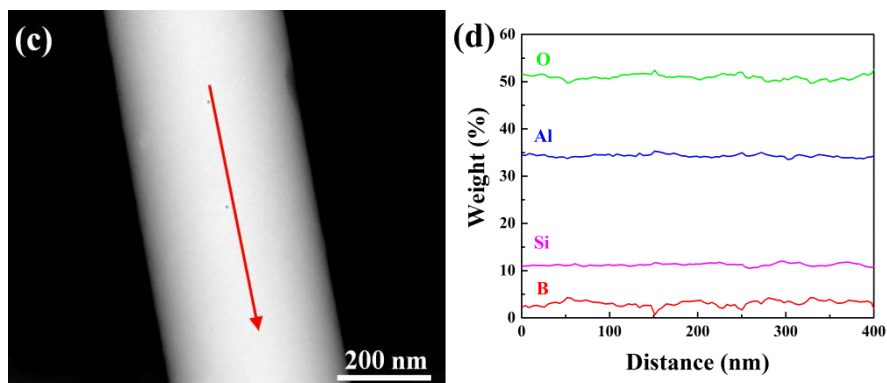
Phase	Card No.	Crystal structure	Lattice parameters		
			$a$ (Å)	$b$ (Å)	$c$ (Å)
$\text{Al}_4\text{B}_2\text{O}_9$	47-0319	Orthorhombic	7.617	7.617	2.827
$\text{Al}_{18}\text{B}_4\text{O}_{33}$	32-0003	Orthorhombic	7.617	15.01	5.664
Mullite	15-0776	Orthorhombic	7.545	7.689	2.884

\* $b$  and  $c$  in  $\text{Al}_{18}\text{B}_4\text{O}_{33}$  are nearly twice as much as that in  $\text{Al}_4\text{B}_2\text{O}_9$  and mullite.

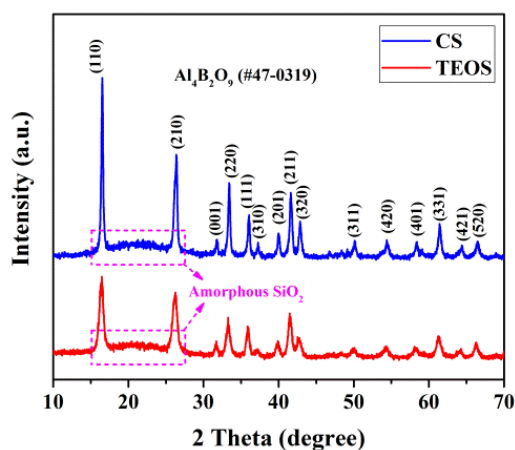


**Fig. 1.** SEM micrographs and diameter distribution histograms for as-spun nanofibers: (a) (b) NF<sub>CS</sub> and (c) (d) NF<sub>TEOS</sub>. The inserts show the surface morphology.

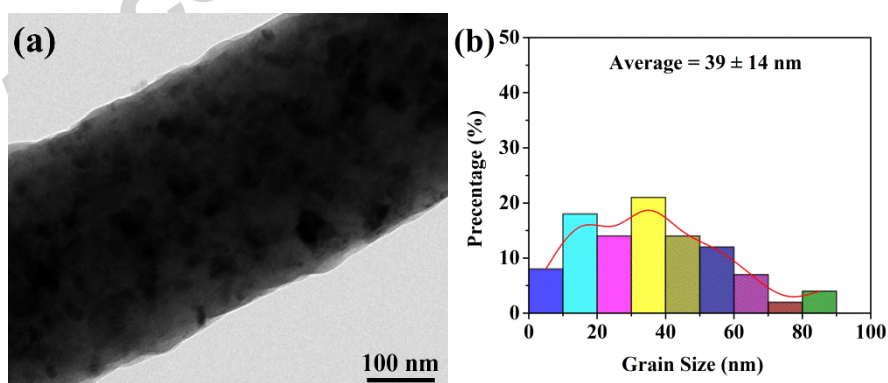




**Fig. 2.** HAADF STEM micrographs and EDS line scan analyses for 3AB2S nanofibers prepared at 800 °C: (a) (b) NF<sub>CS</sub> and (c) (d) NF<sub>TEOS</sub>.



**Fig. 3.** XRD patterns of 3AB2S nanofibers prepared using different sources after calcining at 1000 °C for 3 h.



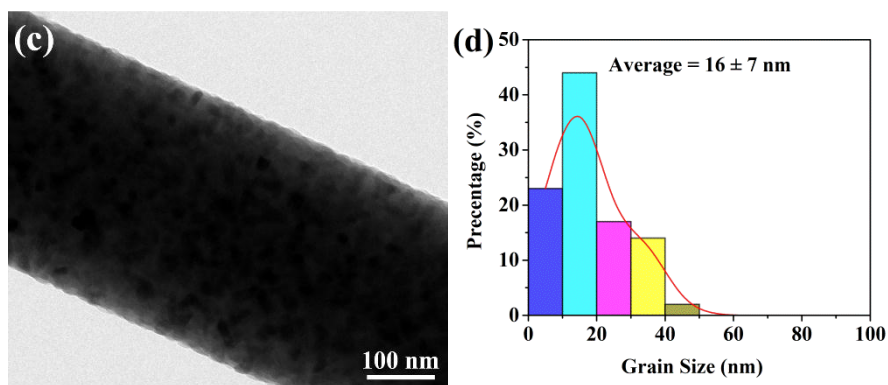


**Fig. 4.** TEM micrographs and grain size distribution histograms for 3AB2S nanofibers: (a) (b)  $\text{NF}_{\text{CS}}$  and (c) (d)  $\text{NF}_{\text{TEOS}}$ .

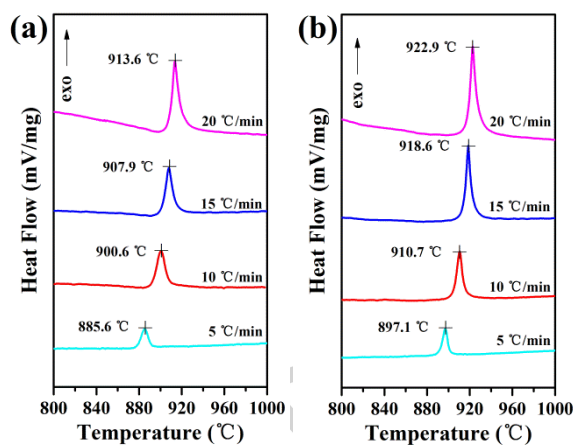


**Fig. 5.** DSC curves of crystalline region for as-spun nanofibers measured at various heating rates: (a)  $\text{NF}_{\text{CS}}$  and (b)  $\text{NF}_{\text{TEOS}}$ .

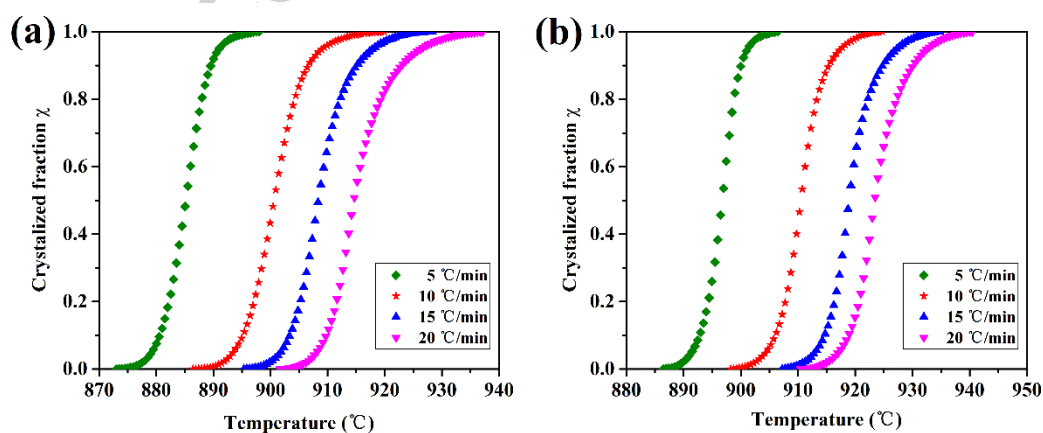


**Fig. 6.** The relationships between  $\chi$  and  $T$  for 3AB2S nanofibers under different heating rates:

(a) NF<sub>CS</sub> and (b) NF<sub>TEOS</sub>.

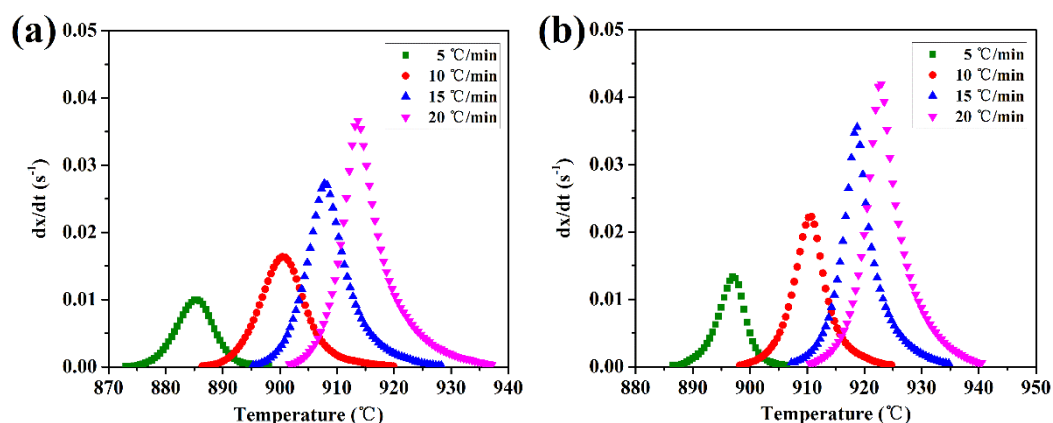


**Fig. 7.** The relationships between  $dx/dt$  and  $T$  for 3AB2S nanofibers under different heating rates: (a) NF<sub>CS</sub> and (b) NF<sub>TEOS</sub>.

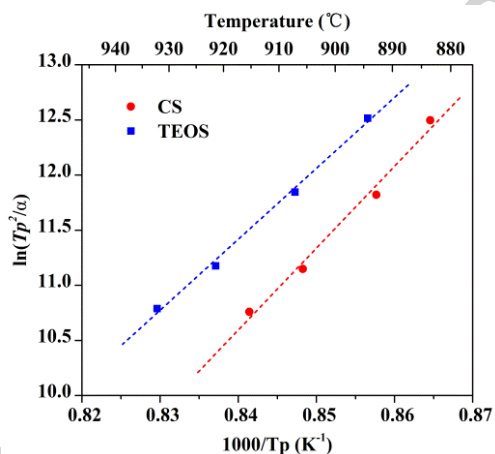


**Fig. 8.** Plots of  $\ln(T_p^2/\alpha)$  versus  $1/T_p$  for the 3AB2S nanofibers prepared using CS and TEOS.

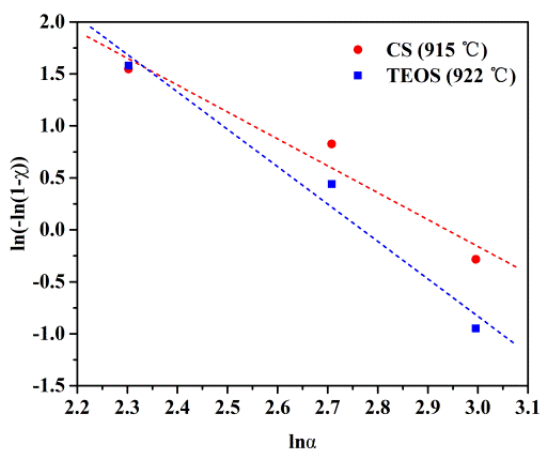


**Fig. 9.** Plots of  $\ln[-\ln(1-\chi)]$  versus  $\ln\alpha$  for the crystalline regions of the 3AB2S nanofibers prepared using CS and TEOS.

Accepted manuscript